ceramics

MDPI

Article

Estimation of Temperature-Dependent Band Parameters for Bi-Doped SnSe with High Thermoelectric Performance

Hyunjin Park †, Sang-il Kim †, Jeong-Yeon Kim, Seong-Mee Hwang and Hyun-Sik Kim *

Department of Materials Science and Engineering, University of Seoul, 163 Seoulsiripdae-ro, Seoul 02504, Republic of Korea
* Correspondence: hyunsik.kim@uos.ac.kr
† These authors contributed equally to this work.

Abstract: Recent studies have revealed the outstanding thermoelectric performance of Bi-doped n-type SnSe. In this regard, we analyzed the band parameters for $Sn_{1-x}Bi_xSe$ (x = 0.00, 0.02, 0.04, and 0.06) using simple equations and the Single Parabolic Band model. Bi doping suppresses the carrier-phonon coupling while increasing the density-of-states effective mass. The n-type SnSe is known to have two conduction bands converge near 600 K. Bi doping changes the temperature at which the band convergence occurs. When x = 0.04, its weighted mobility maximized near 500 K, which indicated the possible band convergence. The highest zT of the x = 0.04 sample at mid-temperatures (473–573 K) can be attributed to the engineered band convergence via Bi doping.

Keywords: thermoelectric; SnSe; *B*-factor; weighted mobility; single parabolic band model

Citation: Park, H.; Kim, S.-i.; Kim, J.-Y.; Hwang, S.-M.; Kim, H.-S. Estimation of Temperature-Dependent Band Parameters for Bi-Doped SnSe with High Thermoelectric Performance. *Ceramics* **2023**, *6*, 504–513. https://doi.org/10.3390/ceramics6010029

Academic Editor: Mari-Ann Einarsrud

Received: 17 December 2022
Revised: 9 February 2023
Accepted: 9 February 2023
Published: 13 February 2023

1. Introduction

Research on various eco-friendly energy technologies has been conducted in various fields to mitigate the acceleration of global warming [1]. In particular, environmentally friendly energy harvesting technologies can play an important role in reducing greenhouse gas emissions, which are a main cause of climate change. Among many environmentally friendly technologies that can harvest energy without consuming fossil fuels, thermoelectric technology is drawing increasing attention because it can convert waste heat into electricity [2]. The conversion efficiency (from waste heat to electricity) of the device is closely coupled with the thermoelectric performance of a material used in the device. The thermoelectric performance of a material is evaluated with a figure of merit, zT, which is defined as $zT = S^2\sigma T/(k_e + k_l)$, where S, σ, T, k_e, and k_l are the Seebeck coefficient, electrical conductivity, absolute temperature, electronic thermal conductivity, and lattice thermal conductivity, respectively. Here, the $S^2\sigma$, termed as the power factor, determines the electronic transport properties of the material [3]. As evident from the equation, a high zT can be achieved by using a material with a high power factor and low thermal conductivity. However, enhancing the power factor is not simple. The S and σ move in the opposite direction when the carrier concentration of a material is controlled with doping or alloying [4–12]. Commonly, several band engineering strategies have been introduced to decouple the trade-off relationship between the S and σ [13–17]. At the same time, materials with an inherently high power factor have been sought.

Kutorasinski et al. found that SnSe, a layered material, has highly anisotropic hole transport properties. Their study showed that p-type SnSe cannot transport charged carriers (holes) in the interlayer, whereas n-type SnSe can do so, thus yielding higher thermoelectric performance. Consequently, n-type SnSe is a better thermoelectric material, owing to its high power factor [4]. Recently, Duong et al. reported n-type Bi-doped SnSe with a maximum zT of 2.2 at 773 K with a high power factor while maintaining a low thermal conductivity [18]. They synthesized Bi-doped SnSe ($Sn_{1-x}Bi_xSe$; x = 0, 0.02, 0.04, and 0.06) and experimentally demonstrated that the power factor of the x = 0.04 sample improved by more than a factor of eleven compared to the pristine SnSe (x = 0) at 572 K. Moreover, an exceptionally high zT of 2.2 was obtained in the x = 0.06 sample at 773 K. Because the total thermal conductivities ($k_e + k_l$) of the x = 0.04 and 0.06 samples are similar, their zTs are closely related to their power factors. With a changing Bi doping content (x), the corresponding σ changed more significantly than their S did. However, the effect of Bi doping on electronic band parameters of $Sn_{1-x}Bi_xSe$ was not provided.

Here, we estimate the band parameters, namely, the density-of-states effective mass (m_d*), non-degenerate mobility (μ_0), weighted mobility (μ_W), and B-factor of $Sn_{1-x}Bi_xSe$ (x = 0, 0.02, 0.04, and 0.06) using the single parabolic band (SPB) model. From how the band parameters change with different Bi doping content, we evaluate the impact of Bi doping on the electronic transport properties of Bi-doped SnSe. At 300 K, Bi doping first decreases the μ_W, which is directly proportional to the theoretical maximum power factor; however, when the x = 0.06, the μ_W is improved by more than a factor of five compared to the pristine SnSe. A drastic increase in the 300 K power factor of the x = 0.06 sample is predicted. The 300 K μ_W improvement is mostly due to the m_d* increase with Bi doping, despite the substantial drop in the μ_0.

2. Materials and Methods

Temperature-dependent S and Hall carrier concentration (n_H) were obtained from the literature [18]. The experimental S and $n_{H,}$ both measured at 300 K, were used to plot the S as a function of n_H. The n_H was converted to chemical carrier concentration (n) using Equation (1) [19].

$$\frac{n}{n_H} = 1.17 - \left[\frac{0.216}{1+\exp\left(\frac{|S|-101}{67.1}\right)}\right] \tag{1}$$

The experimental n-dependent S at 300 K was converted to S-dependent $\log_{10}(n)$ to estimate the m_d*. The m_d* of each sample was estimated by fitting Equation (2) into the experimental data expressed as S-dependent $\log_{10}(n)$ [20].

$$\log_{10}\left(\frac{m_d^*T}{300}\right) = \frac{2}{3}\log_{10}(n) - \frac{2}{3}\left[20.3 - (0.00508 \times |S|) + \left(1.58 \times 0.967^{|S|}\right)\right] \tag{2}$$

Temperature-dependent μ_0 was estimated from the experimental n_H-dependent μ_H at different temperatures using the Single Parabolic Band (SPB) model [21,22]. According to the SPB model under acoustic phonon scattering, the μ_H is defined in terms of μ_0 and reduced fermi level η (Equation (3)).

$$\mu_H = \mu_0 \frac{F_{-1/2}(\eta)}{2F_0(\eta)} \tag{3}$$

The fermi integral of order i (F_i) in Equation (3) is defined as in Equation (4).

$$F_n(\eta) = \int_0^\infty \frac{\varepsilon^n}{1+\exp(\varepsilon-\eta)} d\varepsilon \tag{4}$$

The n_H is defined in terms of m_d* and η (Equation (5)).

$$n_H = \frac{16\pi}{3}\left(\frac{2m_d^*k_BT}{h^2}\right)\frac{(F_0(\eta))^2}{F_{-1/2}(\eta)} \tag{5}$$

Equations (3)–(5) were applied to the experimental n_H-dependent μ_H to estimate μ_0. The temperature-dependent μ_W was calculated using Equation (6) [23].

$$\mu_w = \frac{3h^3\sigma}{8\pi e(2m_ek_BT)^{3/2}}\left[\frac{\exp\left[\frac{|S|}{k_B/e}-2\right]}{1+\exp\left[-5\left(\frac{|S|}{k_B/e}-1\right)\right]} + \frac{\frac{3}{\pi^2}\frac{|S|}{k_B/e}}{1+\exp\left[5\left(\frac{|S|}{k_B/e}-1\right)\right]}\right] \tag{6}$$

The e, m_e, h, and k_B are the electric charge, electron rest mass, Planck constant, and Boltzmann constant, respectively. Finally, the B-factor is estimated using the μ_W and the lattice thermal conductivity (κ_l), as in Equation (7).

$$B = \left(\frac{k_B}{e}\right)^2 \frac{8\pi e(2m_e k_B)^{3/2}}{h^3} \frac{\mu_W T^{5/2}}{\kappa_l} \quad (7)$$

3. Results and Discussion

3.1. Calculation of Density-of-States Effective Mass, m_d*

Figure 1 shows the calculated m_d* for $Sn_{1-x}Bi_xSe$ (x = 0.00, 0.02, 0.04, and 0.06). Figure 1a shows the experimental $|S|$ and n_H for varying x at 300 K expressed in $\log_{10}(n)$ versus $|S|$ graph (in filled symbols). Because we could not measure the n directly, the measured n_H was converted to n using Equation (1) [19]:

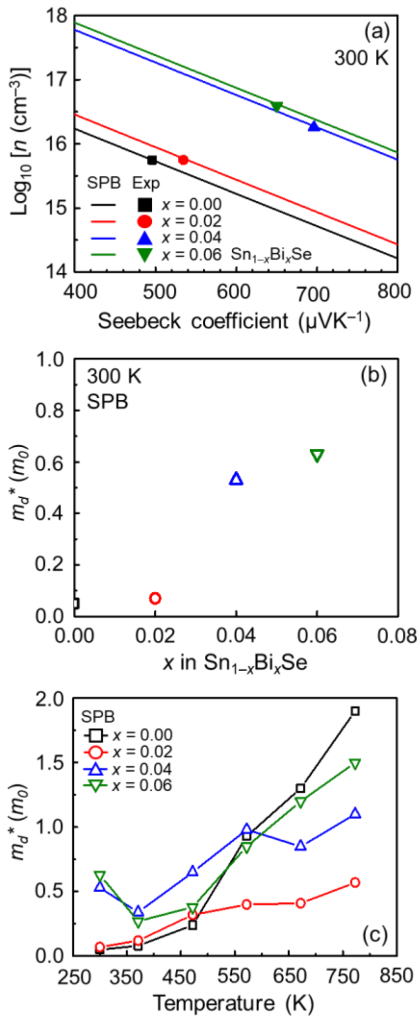

Figure 1. (**a**) Calculated (lines) and experimental (symbols) magnitude of Seebeck coefficient ($|S|$)-dependent $\log_{10}(n)$ for $Sn_{1-x}Bi_xSe$ (x = 0.00, 0.02, 0.04, and 0.06) at 300 K [18], (**b**) calculated density-of-states effective mass (m_d*) varying with x in $Sn_{1-x}Bi_xSe$ (x = 0.00, 0.02, 0.04, and 0.06) at 300 K, and (**c**) calculated m_d* for $Sn_{1-x}Bi_xSe$ (x = 0.00, 0.02, 0.04, and 0.06) varying with temperature (300–773 K).

The ratio of n to n_H is a Hall factor (r_H), and it is a function of η (reduced fermi level). Because the S is determined by the η mathematically according to the SPB model, the r_H can also be expressed in terms of S instead of η. That is the reason why the r_H in Equation (1) is expressed in terms of S. The conversion from the n_H-dependent S to the S-dependent $\log_{10}(n)$ is necessary to accurately estimate the m_d* from it. The simple and accurate equation that enabled us to calculate the m_d* without having to worry about solving the fermi integrals in the SPB model numerically (Equation (4)) was expressed in terms of S and $\log_{10}(n)$, as shown in Equation (2) [20].

When the T, n, and S in units of K, cm^{-3}, and $\mu V\ K^{-1}$ are inserted into Equation (2), the m_d* in the unit of m_e is obtained. While varying S from 400 to 800 $\mu V\ K^{-1}$, the m_d* in Equation (2) is fitted to describe the experimental data in the filled symbols. The results of fitting m_d* using Equation (2) are presented in lines in Figure 1a. From the fact that the filled symbols are on top of the lines of the same color, we can conclude that the fitted m_d* accurately represents the electronic band structure of the samples. From the experimental data (filled symbols), we can see that the n increases with increasing Bi doping content (x). However, the S only increases up to x = 0.04. The S of the x = 0.06 sample is lower than that of the x = 0.04 sample. It is to be noted that the x = 0.00 sample is p-type, while Bi-doped SnSe samples are all n-type. Figure 1b shows the 300 K m_d* for different x. In general, the m_d* increases with an increasing x. The rate of m_d* increase is the most abrupt when the x increases from 0.02 to 0.04, but the m_d* increases from x = 0 to 0.02 or from x = 0.04 to 0.06 are not substantial. As the x increases from 0 to 0.06, the calculated m_d* increases from 0.05 to 0.63 m_e (increasing by more than a factor of twelve). When we assume that there is only one band contributing to the electronic transport properties of $Sn_{1-x}Bi_xSe$ (x = 0.00, 0.02, 0.04, and 0.06), the curvature of the band substantially increases with Bi doping at 300 K. How the m_d* changes with temperature may also be affected by the amount of x. Figure 1c shows the temperature-dependent m_d* for different values of x. Although the m_d* of the x = 0.00 sample is the lowest among other x values at 300 K, it becomes the highest at 773 K. The rate of m_d* change with temperature is different for different x values. Except for the x = 0.00 sample, the rate of m_d* increase increases with an increasing x. Although varying in degree, local peaks are observed near 550–650 K for all x. This can be attributed to the two conduction bands converging near 600 K [24]. Because the two conduction bands converging near 600 K are calculated for n-type SnSe, Bi doping can alter the temperature at which the two conduction bands converge and even the curvature of the two bands. Because we employed the SPB model (only one band contributing to transport), if band convergence occurs, it will be reflected as an increase in the m_d* of the assumed single band.

3.2. Calculation of Non-Degenerate Mobility, μ_0

Figure 2a shows the calculated (lines) and experimental (filled symbols) n_H-dependent μ_H for $Sn_{1-x}Bi_xSe$ (x = 0.00, 0.02, 0.04, and 0.06) at 300 K [18]. The n_H-dependent μ_H calculated using the SPB model (denoted by lines) are in agreement with the experimental data (filled symbols) when the μ_0 is fitted accurately. According to the SPB model, the μ_H and n_H are defined in Equations (3)–(5) [21,22].

To calculate n_H-dependent μ_H, two band parameters needed to be determined: μ_0 (Equation (3)) and m_d* (Equation (5)). By substituting the m_d* we obtained in Figure 1c into Equation 5, only the μ_0 could be estimated by fitting Equations (3)–(5) to the experimental data (filled symbols). The μ_H of the x = 0.00 sample is approximately a factor of 10 greater than those of the Bi-doped samples. When Bi is doped to the x = 0.00 sample, the type of the sample changes from p- to n-type. Once Bi is doped, increasing x also increases the μ_H and n_H, at the same time. The estimated μ_0 at 300 K is shown in Figure 2b. Similar to μ_H, the μ_0 rapidly decreases as Bi doping commences, and subsequently increases with an increase in x. As the Bi-doping concentration, x, increases from 0 to 0.06 in steps of 0.02, μ_0 is calculated to be 11,500, 680, 860, and 1300 $cm^2\ s^{-1}\ V^{-1}$, respectively. The μ_0 is always higher than μ_H, because it represents the μ_H without defects at low degeneracy. The μ_0, in turn, depends on single band mass (related to m_d*) and deformation potential (related to carrier-phonon interaction). The heavier the band mass, the lower the μ_0. If the deformation potential is high, corresponding μ_0 will be low. Because Bi doping increases the m_d* at 300 K (Figure 1b), from the fact that Bi doping also increases the μ_0 at 300 K (Figure 2b) we can suggest that the interaction between the charged carriers and the phonons decreases with Bi doping at 300 K (favorable to electronic transport). The estimated μ_0 with temperature is plotted in Figure 2c. The increasing carrier-phonon scattering at high temperatures and the m_d* (Figure 1c) are responsible for the drop in μ_0 with temperatures. Among Bi-doped samples, unlike the x = 0.02 sample whose μ_0 decreases with temperatures, the μ_0 of x = 0.04 and 0.06 samples peak near 373 K. With the exception of 300 and 773 K, the μ_0 of x = 0.04 are higher than those of the x = 0.06 sample at all temperatures. Different trends observed in the temperature-dependent μ_0 can be understood in terms of how the m_d* and deformation potential of the samples change with temperatures. At 773 K, SnSe has the lowest μ_0 of 6.4 cm^2 s^{-1} V^{-1}, whereas $Sn_{1-x}Bi_xSe$, with x = 0.02, 0.04, and 0.06, have μ_0 of 13, 21, and 22 cm^2 s^{-1} V^{-1}, respectively.

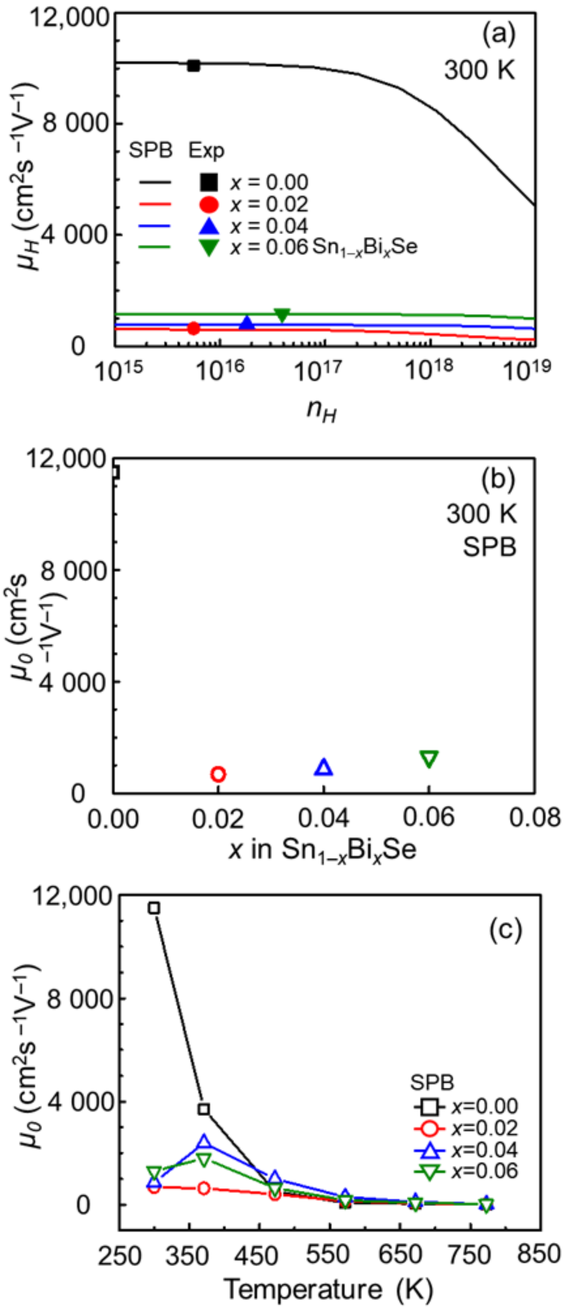

Figure 2. (**a**) Calculated (lines) and experimental (symbols) n_H-dependent Hall mobility (μ_H) for $Sn_{1-x}Bi_xSe$ (x = 0.00, 0.02, 0.04, and 0.06) at 300 K [18], (**b**) calculated non-degenerate mobility (μ_0) varying with x in $Sn_{1-x}Bi_xSe$ (x = 0.00, 0.02, 0.04, and 0.06) at 300 K, and (**c**) calculated μ_0 for $Sn_{1-x}Bi_xSe$ (x = 0.00, 0.02, 0.04, and 0.06) varying with temperature (300–773 K).

3.3. Calculation of Weighted Mobility, μ_W

Figure 3 presents μ_W calculated from experimental σ, S, and T using Equation (6) [23]. Figure 3a shows μ_W calculated at 300 K.

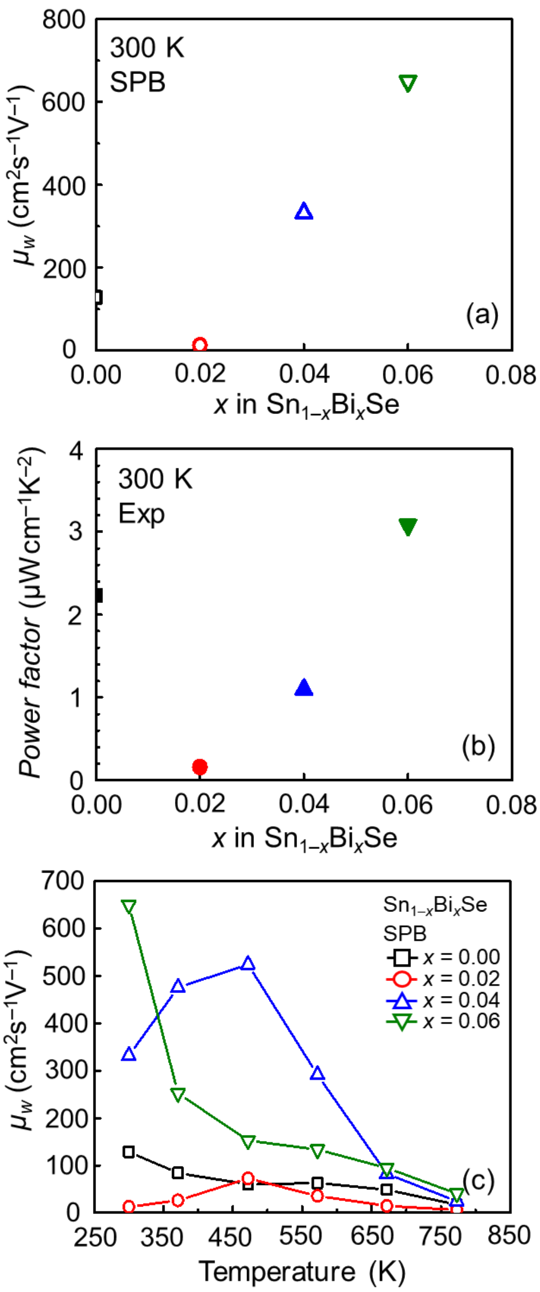

Figure 3. (**a**) Calculated weighted mobility (μ_W) varying with x in $Sn_{1-x}Bi_xSe$ (x = 0.00, 0.02, 0.04, and 0.06) at 300 K, (**b**) experimental power factor varying with x in $Sn_{1-x}Bi_xSe$ (x = 0.00, 0.02, 0.04, and 0.06) at 300 K [18], and (**c**) calculated μ_W for $Sn_{1-x}Bi_xSe$ (x = 0.00, 0.02, 0.04, and 0.06) varying with temperature (300–773 K).

At 300 K, the calculated μ_W is highest when x = 0.06 (~650 $cm^2\ s^{-1}\ V^{-1}$). Physically, the μ_W is defined as a product between μ_0 and $(m_d^*/m_e)^{3/2}$, and it is directly proportional to the maximum power factor of a sample. The theoretically maximum power factor can be obtained when the n_H of the sample is optimally tuned. Hence, when the band parameter, μ_W, of different samples are compared, a more promising sample (or composition) can be easily chosen. Therefore, the x = 0.06 sample with the highest μ_W at 300 K tells us that the

$x = 0.06$ sample will exhibit the highest power factor among other samples once its n_H is at its optimum. The experimental power factor of $Sn_{1-x}Bi_xSe$ (x = 0.00, 0.02, 0.04, and 0.06) at 300 K is provided in Figure 3b [18]. The plotted values in Figure 3a,b form similar V-shaped graphs. As the x in $Sn_{1-x}Bi_xSe$ varies from 0 to 0.02, μ_W and the power factor decrease. Subsequently, as x varies from 0.02 to 0.06, μ_W and the power factor increase. The trends in μ_W and power factor can be different from each other. The fact that both trends in μ_W (Figure 3a) and power factor (Figure 3b) are comparable tells us that the n_H of all samples are not far from their optimum n_H. Figure 3c shows the variation in μ_W with temperature, which is also obtained by Equation (6). The μ_W can also be used to see if there is any band convergence benefitting the electronic transport properties. The μ_W of the $x = 0.02$ and 0.04 samples peaks near 473 K. The highest μ_W of $x = 0.06$ is estimated to be near 300 K, but the rate of μ_W drop with temperature also decreases near 473 K. We believe that the electronic transport properties' improvement in Bi-doped SnSe due to band convergence is the strongest near 473 K. However, experimentally, the power factor of the $x = 0.04$ sample is the highest near 573 K [18]. However, if the n_H at 473 K is optimized, the power factor of the $x = 0.04$ sample at 473 K will be higher than that at 573 K.

3.4. Calculation of B-Factor

Figure 4 shows the calculated B-factor and the corresponding measured zT at 300 K [18]. The B-factor values shown in Figure 4a are calculated based on the μ_W in Figure 3 and the experimental κ_l [18] using Equation (7) [25–30]:

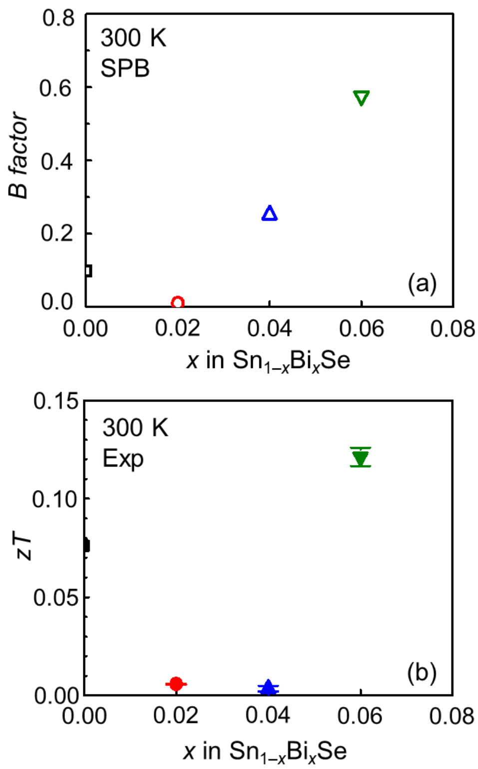

Figure 4. (**a**) Calculated B-factor varying with x in $Sn_{1-x}Bi_xSe$ (x = 0.00, 0.02, 0.04, and 0.06) at 300 K, (**b**) experimental zT varying with x in $Sn_{1-x}Bi_xSe$ (x = 0.00, 0.02, 0.04, and 0.06) at 300 K [18].

The trend observed in the B-factor (Figure 4a) is similar to that observed in μ_W in Figure 3a. The B-factor first decreases with Bi doping, but with increasing x (Bi doping content), the corresponding B-factor increases. The B-factor when $x = 0.02$, which is almost 0, improves to ~0.58 when $x = 0.06$. The fact that the trend in the x-dependent B-factor is similar to that observed in the x-dependent μ_W tells us that the 300 K κ_l of the $Sn_{1-x}Bi_xSe$ are also similar to each other. If the discrepancy in κ_l among the samples with a different

x is large, the x-dependent μ_W must have been changed in the x-dependent B-factor. The 300 K B-factor when x = 0.06 is almost a factor of six greater than that of the undoped SnSe (p-type). Although the μ_W is directly proportional to the theoretical maximum power factor, the B-factor is not exactly proportional to the theoretical maximum zT. However, the B-factor is related to the theoretical maximum zT. Because the B-factor of the x = 0.06 sample has the highest B-factor, we also expect the highest 300 K zT in the x = 0.06 sample if its n_H is not too far from the optimum n_H. Figure 4b shows the experimental 300 K zT for different x values, and as predicted in Figure 4a, the zT of the x = 0.06 sample exhibits the highest zT of 0.12 [18]. Experimentally, the 300 K zT of the x = 0.02 and 0.04 are comparable (zT~0.005). However, the 300 K B-factor of the x = 0.04 sample is much higher than that of the x = 0.02 sample. In other words, once the n_H is appropriately tuned, the 300 K zT when x = 0.04 can be improved to be much higher than zT of 0.05.

Figure 5 shows the temperature-dependent B-factor and corresponding measured zT. Although, the B-factor when x = 0.04 is lower than that when x = 0.06 at 300 K. For temperatures from 373 to 573 K, the B-factor of the x = 0.04 sample is the highest among other samples. However, the B-factor of the x = 0.06 sample is highest at temperatures higher than 673 K. Initially, the μ_W of the x = 0.04 sample was the highest for temperatures from 373 to 573 K, with a peak μ_W at 473 K (Figure 3c). In terms of the B-factor, the peak B-factor is observed at 573 K. This shift of the peak temperature when comparing the temperature μ_W and B-factor originates from the κ_l decreasing with temperature. Only the zT of the x = 0.04 sample at 473 and 573 K are the highest, while its B-factor is the highest from 373 to 573 K. Upon n_H tuning, the zT of the x = 0.04 sample at 373 K can be much higher than that observed for the x = 0.06 sample at 373 K. Bi doping in SnSe is an effective strategy to improve its mid-temperature zT, as Bi doping can engineer band convergence to maximize its thermoelectric performance.

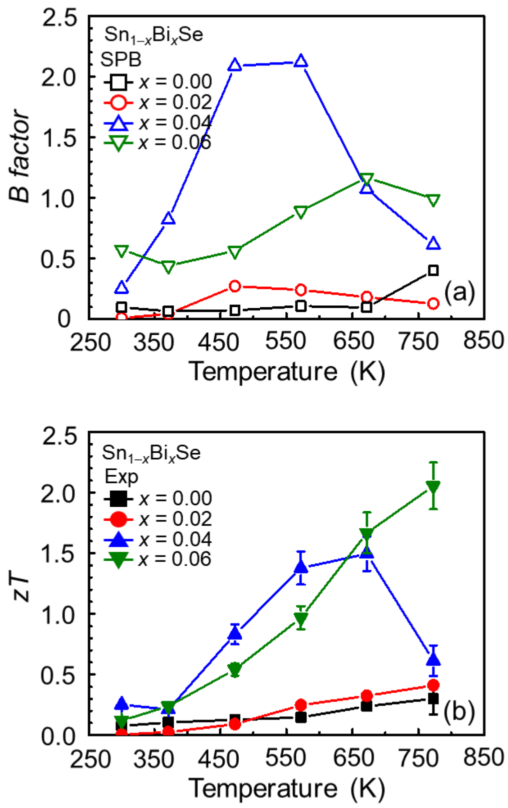

Figure 5. (**a**) Calculated temperature-dependent B-factor varying with x in $Sn_{1-x}Bi_xSe$ (x = 0.00, 0.02, 0.04, and 0.06), (**b**) experimental temperature-dependent zT varying with x in $Sn_{1-x}Bi_xSe$ (x = 0.00, 0.02, 0.04, and 0.06) [18].

4. Conclusions

Bi doping transforms SnSe from p-type to n-type, resulting in its high thermoelectric performance. In this study, we calculated four band parameters (density-of-states effective mass (m_d*), non-degenerate mobility (μ_0), weighted mobility (μ_W), and the *B*-factor) for $Sn_{1-x}Bi_xSe$ (x = 0.00, 0.02, 0.04, and 0.06) using simple equations and the Single Parabolic Band model. Bi doping can increase both the m_d* and the μ_0 at the same time to improve the electronic transport properties. The physical reason behind the simultaneous improvement in m_d* and the μ_0 with Bi doping can be attributed to suppressed carrier-phonon interaction. Bi doping also changes how the band parameters change with temperature. The two conduction bands in n-type SnSe known to converge near 600 K now converge near 500 K when x = 0.04. The existence of the band convergence is confirmed by the temperature at which the μ_W peaks. Due to the two conduction bands converging near 500 K in the x = 0.04 sample, the zT of the x = 0.04 sample is highest for temperatures between 473 and 573 K.

Author Contributions: Conceptualization, H.P. and S.-i.K.; validation, S.-i.K.; formal analysis, H.P. and S.-M.H.; writing—original draft preparation, H.P. and S.-i.K.; writing—review and editing, H.-S.K.; visualization, J.-Y.K.; supervision, H.-S.K.; funding acquisition, H.-S.K. All authors have read and agreed to the published version of the manuscript.

Funding: This work was financially supported by the National Research Foundation of Korea (NRF), funded by the Ministry of Education (NRF-2021K2A9A1A06092290).

Data Availability Statement: The data presented in this study are available on request from the corresponding author.

Conflicts of Interest: The authors declare no conflict of interest.

References

1. Cenci, M.P.; Scarazzato, T.; Munchen, D.D.; Dartora, P.C.; Veit, H.M.; Bernardes, A.M.; Dias, P.R. Eco-Friendly Electronics-A Comprehensive Review. *Adv. Mater. Technol.* **2021**, *7*, 2001263. [CrossRef]
2. Lee, J.; Kim, D.H.; Lee, S.T.; Lim, J.K. Fundamental Study of Energy Harvesting Using Thermoelectric Effect on Concrete Structure in Road. *Adv. Mater. Res.* **2014**, *1044–1045*, 332–337. [CrossRef]
3. Wei, J.; Yang, L.; Ma, Z.; Song, P.; Zhang, M.; Ma, J.; Yang, F.; Wang, X. Review of current high-ZT thermoelectric materials. *J. Mater. Sci.* **2020**, *55*, 12642–12701. [CrossRef]
4. Kutorasinski, K.; Wiendlocha, B.; Kaprzyk, S.; Tobola, J. Electronic structure and thermoelectric properties of n- and p-type SnSe from first principles calculations. *Phys. Rev. B* **2015**, *91*, 205201. [CrossRef]
5. Lee, K.H.; Kim, Y.-M.; Park, C.O.; Shin, W.H.; Kim, S.W.; Kim, H.-S.; Kim, S.-I. Cumulative defect structures for experimentally attainable low thermal conductivity in thermoelectric $(Bi,Sb)_2Te_3$ alloys. *Mater. Today Energy* **2021**, *21*, 100795. [CrossRef]
6. Cai, S.; Hao, S.; Luo, Y.; Su, X.; Luo, Z.-Z.; Hu, X.; Wolverton, C.; Dravid, V.P.; Kanatzidis, M.G. Ultralow Thermal Conductivity and Thermoelectric Properties of $Rb_2Bi_8Se_{13}$. *Chem. Mater.* **2020**, *32*, 3561–3569. [CrossRef]
7. Pei, Y.; Lensch-Falk, J.; Toberer, E.S.; Medlin, D.L.; Snyder, G.J. High Thermoelectric Performance in PbTe Due to Large Nanoscale Ag2Te Precipitates and La Doping. *Adv. Funct. Mater.* **2011**, *21*, 241–249. [CrossRef]
8. Zhang, X.; Zhao, L.-D. Thermoelectric materials: Energy conversion between heat and electricity. *J. Mater.* **2015**, *1*, 92–105. [CrossRef]
9. Banik, A.; Shenoy, U.S.; Anand, S.; Waghmare, U.V.; Biswas, K. Mg Alloying in SnTe Facilitates Valence Band Convergence and Optimizes Thermoelectric Properties. *Chem. Mater.* **2015**, *27*, 581–587. [CrossRef]
10. Takagiwa, Y.; Pei, Y.; Pomrehn, G.; Snyder, G.J. Dopants effect on the band structure of PbTe thermoelectric material. *Appl. Phys. Lett.* **2012**, *101*, 092102. [CrossRef]
11. Ding, G.; Si, J.; Yang, S.; Wang, G.; Wu, H. High thermoelectric properties of n-type Cd-doped PbTe prepared by melt spinning. *Scr. Mater.* **2016**, *122*, 1–4. [CrossRef]
12. Zhai, H.; Xiao, Y.; Zhao, L.-D.; Tan, G.; Tang, X. Large effective mass and low lattice thermal conductivity contributing to high thermoelectric performance of Zn-doped Cu5Sn2Se7. *J. Alloys Compd.* **2020**, *826*, 154154. [CrossRef]
13. Lee, Y.K.; Luo, Z.; Cho, S.P.; Kanatzidis, M.G.; Chung, I. Surface Oxide Removal for Polycrystalline SnSe Reveals Near-Single-Crystal Thermoelectric Performance. *Joule* **2019**, *3*, 719–731. [CrossRef]
14. Sales, B.C.; Mandrus, D.; Williams, R.K. Filled Skutterudite Antimonides: A New Class of Thermoelectric Materials. *Science* **1996**, *272*, 1325–1328. [CrossRef] [PubMed]
15. Li, W.; Xu, T.; Ma, Z.; Cheng, Y.; Li, J.; Jiang, Q.; Luo, Y.; Yang, J. High thermoelectric performance in p-type InSb with all-scale hierarchical architectures. *Mater. Today Energy* **2022**, *29*, 101091. [CrossRef]

16. Jang, H.; Toriyama, M.Y.; Abbey, S.; Frimpong, B.; Male, J.P.; Snyder, G.J.; Jung, Y.S.; Oh, M.-W. Suppressing Charged Cation Antisites via Se Vapor Annealing Enables p-Type Dopability in $AgBiSe_2$–SnSe Thermoelectrics. *Adv. Mater.* **2022**, *34*, 2204132. [CrossRef] [PubMed]
17. Shi, X.-L.; Zou, J.; Chen, Z.-G. Advanced thermoelectric design: From materials and structures to device. *Chem. Rev.* **2020**, *120*, 7399–7515. [CrossRef] [PubMed]
18. Duong, A.T.; Nguyen, V.Q.; Duvjir, G.; Duong, V.T.; Kwon, S.; Song, J.Y.; Lee, J.K.; Lee, J.E.; Min, T.; Lee, J.; et al. Achieving ZT = 2.2 with Bi-doped n-type SnSe single crystals. *Nat. Commun.* **2016**, *7*, 13713. [CrossRef]
19. Lim, J.-C.; Kim, S.Y.; Shin, W.H.; Kim, S.-I.; Roh, J.W.; Yang, H.; Kim, H.-S. Characterization of Hall factor with Seebeck coefficient measurement. *ACS Appl. Energy Mater.* **2022**, *5*, 4036. [CrossRef]
20. Lee, K.H.; Kim, S.-I.; Lim, J.-C.; Cho, J.Y.; Yang, H.; Kim, H.-S. Approach to Determine the Density-of-States Effective Mass with Carrier Concentration-Dependent Seebeck Coefficient. *Adv. Funct. Mater.* **2022**, *32*, 2203852. [CrossRef]
21. May, A.F.; Snyder, G.J. Introduction to modeling thermoelectric transport at high temperatures. In *Thermoelectrics and Its Energy Harvesting*; Rowe, D.M., Ed.; CRC Press: London, UK, 2012; Volume 1, pp. 1–18.
22. Kim, M.; Kim, S.-I.; Kim, S.W.; Kim, H.-S.; Lee, K.H. Weighted Mobility Ratio Engineering for High-Performance Bi–Te-Based Thermoelectric Materials via Suppression of Minority Carrier Transport. *Adv. Mater.* **2021**, *33*, 2005931. [CrossRef] [PubMed]
23. Snyder, G.J.; Snyder, A.H.; Wood, M.; Gurunathan, R.; Snyder, B.H.; Niu, C. Weighted Mobility. *Adv. Mater.* **2020**, *32*, 2001537. [CrossRef] [PubMed]
24. Chang, C.; Wu, M.; He, D.; Pei, Y.; Wu, C.-F.; We, X.; Yu, H.; Zhu, F.; Wang, K.; Chen, Y.; et al. 3D charge and 2D phonon transports leading to high out-of-plane ZT in n-type SnSe crystals. *Science* **2018**, *360*, 778. [CrossRef]
25. Witting, I.T.; Chasapis, T.C.; Ricci, F.; Peters, M.; Heinz, N.A.; Hautier, G.; Snyder, G.J. The Thermoelectric Properties of Bismuth Telluride. *Adv. Electron. Mater.* **2019**, *5*, 1800904. [CrossRef]
26. Wang, H.; Pei, Y.; LaLonde, A.D.; Snyder, G.J. Material design considerations based on thermoelectric quality factor. In *Thermoelectric Nanomaterials*; Kumoto, K., Mori, T., Eds.; Springer: Berlin, Germany, 2013; pp. 1–32.
27. Pei, Y.; Wang, H.; Snyder, G.J. Band Engineering of Thermoelectric Materials. *Adv. Mater.* **2021**, *4*, 6125. [CrossRef] [PubMed]
28. Pei, Y.; LaLonde, A.D.; Wang, H.; Snyder, G.J. Low effective mass leading to high thermoelectric performance. *Energy Environ. Sci.* **2012**, *5*, 7963. [CrossRef]
29. Zhang, X.; Bu, Z.; Shi, X.; Chen, Z.; Kin, S.; Shan, B.; Wood, M.; Snyder, A.H.; Chen, L.; Snyder, G.J.; et al. Electronic quality factor for thermoelectrics. *Sci. Adv.* **2020**, *6*, eabc0726. [CrossRef]
30. Devlin, K.P.; Chen, S.; Donadio, D.; Kauzlarich, S.M. Solid Solution Yb2–xCaxCdSb2: Structure, Thermoelectric Properties, and Quality Factor. *Inorg. Chem.* **2021**, *60*, 13596. [CrossRef]